

Interannual variations in nutrient supply in the East China Sea influenced by the Zhejiang coastal upwelling and Kuroshio intrusion

Yifei Luo^{1,2}, Jie Shi^{1,2}, Xinyu Guo³, Xinyan Mao⁴, Peng Yao^{2,5}, Bin Zhao^{2,5}, Lin Chen^{2,5}, and Yucheng Wang⁶

¹ Key Laboratory of Marine Environment and Ecology, Ocean University of China, Ministry of Education, 238 Songling Road, Qingdao 266100, China.

² Laboratory for Marine Ecology and Environmental Sciences, Qingdao National Laboratory for Marine Science and Technology, Qingdao 266237, China.

³ Center for Marine Environmental Studies, Ehime University, 2-5 Bunkyo-cho, Matsuyama 790-8577, Japan.

⁴ College of Oceanic and Atmospheric Sciences, Ocean University of China, Qingdao 266100, China.

⁵ Frontiers Science Center for Deep Ocean Multispheres and Earth System, and Key Laboratory of Marine Chemistry Theory and Technology, Ministry of Education, Ocean University of China, Qingdao 266100, China.

⁶ High Performance Computing Center, Pilot National Laboratory for Marine Science and Technology (Qingdao), Qingdao 266237, China.

Corresponding author: Jie Shi (shijie@ouc.edu.cn)

Key Points:

- A strong upwelling year and a weak upwelling year are identified from 2010 to 2018 based on model results and observations.
- Coastal upwelling and Kuroshio intrusion mainly control the nutrient supply in nearshore and offshore areas, respectively.
- Nearshore chlorophyll-*a* and offshore subsurface chlorophyll maximum are accordingly determined by ZCU and KI intensities, respectively.

Abstract

The East China Sea (ECS) is a marginal sea with high productivity, especially in the summer. In the Zhejiang coastal region of the ECS, the large local phytoplankton biomass in summer is attributed to the nutrients pumped up by Zhejiang coastal upwelling (ZCU), and oceanic nutrients supplied by the Kuroshio intrusion (KI) onto the continental ECS. However, the interannual variations in these two processes are not consistent, which complicates coastal nutrient supplies. In this study, to distinguish the contributions of ZCU and KI to the interannual variations of nutrient supplies, nutrient concentrations, and phytoplankton biomass, a physical-biochemical coupled model was applied. According to the model results and observations, the years 2013 and 2018 were identified as strong and weak ZCU years within the 2010–2018 period, respectively. In 2013, nutrient and chlorophyll-*a* concentrations were higher than 2018 in coastal areas, but nutrient concentrations were lower than 2018 at the bottom of wide offshore areas. Strong wind stress in 2013 induced strong ZCU and shoreward net nutrient flux along the 60-m isobath, which was seaward in 2018. The fewer nutrient supplies from KI in the spring of 2013 decreased the nutrient concentrations at the bottom of offshore areas, but its influence on nearshore nutrient concentrations was not as obvious as that caused by ZCU. Phytoplankton biomass in the nearshore and offshore areas reflected different mechanisms of nutrient supplies. In conclusion, the intensity of ZCU, rather than KI, is the principal factor influencing the coastal primary productivity of the ECS in summer.

Plain Language Summary

The Zhejiang coastal region in the East China Sea is one of the most important fishing grounds in China. The highest productivity in this region appears in summer. It is reported that the coastal productivity benefit from the nutrients transported by local upwelling in summer and Kuroshio intrusion from the open sea in spring. To reveal the contributions of the two processes, we used a numerical model to investigate the nutrient supply and phytoplankton biomass influenced by the upwelling and Kuroshio intrusion. The results showed that the more intense alongshore wind in summer induced stronger upwelling, and significantly increased nutrient supply in nearshore areas. The Kuroshio intrusion mainly influenced the nutrient supply from the open sea and the nutrient concentrations in offshore areas at the sea bottom. The nearshore nutrient supply and phytoplankton biomass are primarily determined by the intensity of upwelling and secondarily influenced by that of Kuroshio intrusion. This study distinguished the effects of local and remote processes, and highlighted the contributions of the local process at an interannual time scale.

1 Introduction

Upwelling is a worldwide phenomenon that transports deep cold water to the upper layers and decreases sea surface temperature (SST; Jing et al., 2011; Xie & Hsieh, 1995). Deep nutrient-rich water is pumped up to the euphotic layers, thereby promoting local primary production and the associated species interactions (Capone & Hutchins, 2013; Hu & Wang, 2016; Menge & Menge, 2013). Upwelling systems are widely distributed in open oceans. In the Eastern Boundary Upwelling Systems, upwelling induced by alongshore winds appear over a wide range of latitudes in coastal areas (Sydeman et al., 2014; Wang et al., 2015). Marine fish caught in these upwelling regions account for 20% of the fish caught globally (Fréon et al., 2009). In equatorial regions, upwelling generated by trade winds can decrease iron limitation and promote primary

production (Strutton et al., 2004). In some marginal seas, upwelling induced by local seasonal winds (e.g., the Asian monsoon) also plays an important role in regulating biological productivity. In the western Arabian Sea, the area of water with high biomass caused by the Oman Coastal Upwelling extends up to 700 km offshore (Barber et al., 2001). Correlations between upwelling and biological production are also found in many other marginal seas, such as that south of Madagascar (Ramanantsoa et al., 2018), the eastern Great Australian Bight (van Ruth et al., 2018), the southwestern Japan Sea (Hahm et al., 2019), and the East China Sea (ECS; Hu et al., 2014).

Many quantitative indices, defined by the causes or effects of upwelling, have been used to describe the intensity of upwelling. Bakun (1973) introduced a coastal upwelling index based on wind-induced Ekman transport and evaluated the temporal and spatial variations in upwelling along the west coast of North America. Bograd et al. (2009) further developed this index and found a delayed and weak upwelling in El Niño years in the California Current System. The Ekman pumping induced by wind stress curl is also an important cause of upwelling in some regions, such as the Peru Current System (Albert et al., 2010) and the South China Sea (Wang et al., 2013). The effects of upwelling, such as lower SST and higher chlorophyll-*a* (Chl-*a*) concentration, were also used to determine the intensity of the upwelling. The weakening upwelling in the northern Arabian Sea is indicated by an increase in SST and a decrease in Chl-*a* concentration (Lahiri & Vissa, 2022). Using the difference in SST between the upwelling area and the surrounding area, the lifecycle of short-term upwelling processes northeast of Taiwan was determined to be approximately 15 ± 5 days (Yin & Huang, 2019). Using these indices, it was found that upwelling in the low-latitude regions of Eastern Boundary Upwelling Systems exists almost year-round (Wang et al., 2015), but the upwelling induced by monsoons only exists in a certain season when the wind field favors its formation (Ningsih et al., 2013; Villanoy et al., 2011).

The intensity of upwelling presents interannual variations that are important for biological production. The interannual variability of seasonal upwelling was found to be greater than that of existing year-round upwelling (Nykjær & Van Camp, 1994). Sun et al. (2016) suggested that El Niño-Southern Oscillation (ENSO) and Pacific Decadal Oscillation (PDO) could enhance or weaken the summer monsoon in the ECS, respectively, and also affect the intensity of upwelling. Using numerical simulations, Jacox et al. (2015) pointed out that wind and remote forcings (e.g., ENSO and PDO) drive the interannual fluctuations of the upwelled nitrate flux in the California Current System. In the South China Sea, an abnormally strengthened coastal upwelling, indicated by satellite-derived SST, was the reason for an unusual coastal phytoplankton bloom in the summer of 2018 (Hu et al., 2021). Along the northwestern coast of the Iberian Peninsula, Picado et al. (2014) found that summer upwelling was strong during the years with the highest Chl-*a* concentrations (over 7 mg/m³).

The ECS (Fig. 1) is a marginal sea in the northwestern Pacific Ocean, with high biological productivity (Shan et al., 2011; Tan & Shi, 2006). In summer, the southwest monsoon creates favorable conditions for the northeastward alongshore current and the occurrence of the Zhejiang coastal upwelling (ZCU; Gan et al., 2016; Hu et al., 2016; Liu et al., 2021a). Both satellite-

derived data and numerical simulations indicate that the ZCU occurs in nearshore areas within the 60-m isobath in summer (Lou et al., 2011; Lü et al., 2007). Although the ZCU is close to the Changjiang River, the largest river in China, the discharged nutrient-rich freshwater mainly flows northeastward, away from the ZCU (Liu et al., 2021b). The Kuroshio intrusion (KI) on the continental shelf of the ECS is the major nutrient source of the ZCU, particularly a phosphate source. The coastal ECS is dominated by N-rich water and exhibits P-limitation (Wang, 2006; Wang et al., 2003). A nearshore branch current with a low N/P ratio originates from the Kuroshio subsurface water northeast of Taiwan (NKBC in Fig. 1b) and intrudes into the ECS continental shelf (Yue et al., 2021; Zhou et al., 2018). In climatological numerical experiments, the NKBC extends shoreward and northeastward, and reaches the Zhejiang coastal region in summer (Xu et al., 2018; Yang et al., 2011). The ZCU then transports this water with a low N/P ratio to the sea surface, which relieves P-limitation and promotes primary production (Xu et al., 2020). Evidence of upwelled P-rich water was also found through in situ observations (Chen et al., 2021; Wang & Wang, 2007). Therefore, the ZCU and KI, two successive processes, jointly supply nutrients to the Zhejiang coastal region when ZCU occurs.

The intensities of the ZCU and KI are both characterized by obvious interannual variations. As indicated by satellite-derived SST, the maximum cold-water coverage of the ZCU in a year varies from 17000 km² to 25000 km² (Lou et al., 2011). Through numerical simulation, it was found that the transport of phosphate from KI to the continental ECS varies from -0.25 kmol/s to 0.30 kmol/s, which is attributed to the shift of the Kuroshio axis (Lin et al., 2019). However, according to previous studies, the interannual variations in the intensities of these two processes seem inconsistent. As revealed by SST-derived indices, the intensity of the ZCU demonstrated a decreasing trend in the period 1993–2007 (Yang et al., 2020). The intensity of KI, as indicated by the onshore flux, showed an increasing trend during the same period (Li et al., 2013). In addition, the most intense years for the two processes were different. Such inconsistency probably affects the nutrient supply to the ECS shelf as well as coastal primary production, which cannot be determined by climatological research. However, this inconsistency has not drawn sufficient attention, and the contributions of these two processes have not yet been investigated.

In this study, a three-dimensional physical-biochemical coupled model was used to distinguish the effects of ZCU and KI on nutrient supply and phytoplankton biomass in the ECS. Section 2 describes the model and observation data. Section 3 presents the distributions of the water temperature, vertical velocity, nutrients, and Chl-*a* concentrations. Section 4 discusses the contributions of the ZCU and KI to nutrient fluxes and phytoplankton biomass, and the factors controlling the two processes. Finally, a summary of the study is presented in Section 5.

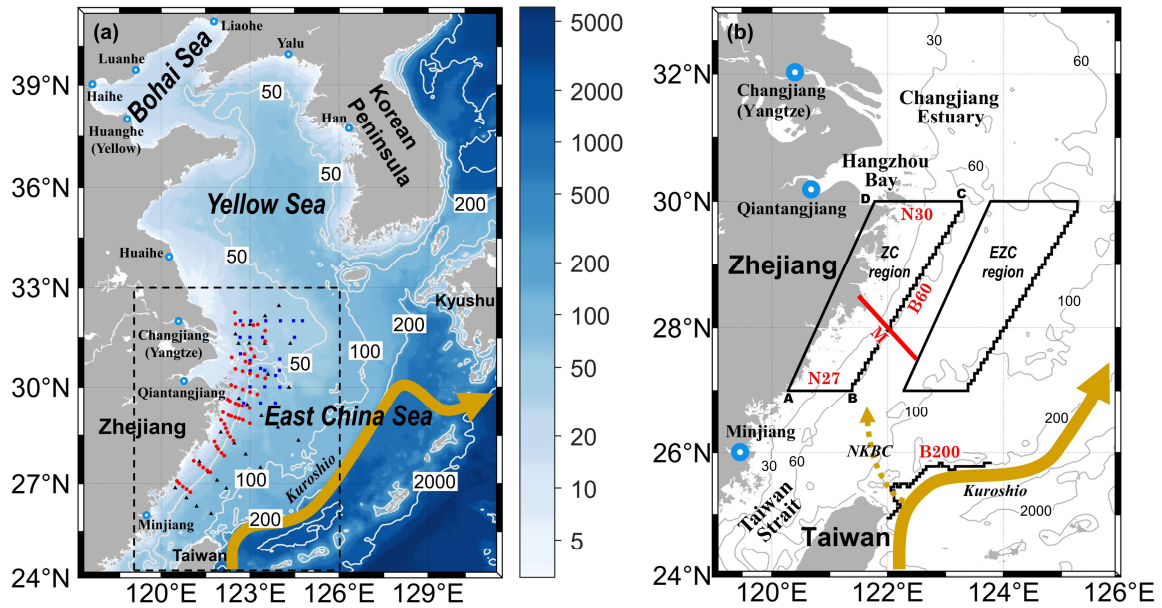


Figure 1. (a) Map of the model domain and (b) enlarged coastal East China Sea (ECS). Scatters in (a) denote coastal nutrient sampling sites in the summer of 2013 and 2018, among which red circles are the sites of this study, blue squares are the sites from Yu (2014), black triangles are the sites from Lyu et al. (2020). Blue-white dots in (a, b) are the positions of inflow from rivers. ZC region: Zhejiang coastal region, EZC region: East Zhejiang coastal region, NKBC: nearshore Kuroshio Branch Current. Sections N27, B60, and N30 are the open boundaries of the ZC region. A, B, C, and D represent the endpoints of the sections N27, B60, and N30. Section M is a cross-shelf section. Section B200 is the location where NKBC intrudes into the ECS. The gray lines represent the isobaths.

2 Methods

2.1 Model description

The three-dimensional physical-biochemical coupled model used in this study consists of two modules. The physical module is based on the Princeton Ocean Model (Blumberg & Mellor, 1987; Mellor, 2003), and the biochemical module is based on the biological part of the NORWECOM (Skogen & S iland, 1998). The physical module provides the water temperatures, current velocities, and turbulent viscosity coefficient to the biochemical module. There are seven state variables in the biochemical module: dissolved inorganic nitrogen (DIN), dissolved inorganic phosphorus (DIP), silicate, diatoms, flagellates, detritus, and biogenic silica. The biomass of both diatoms and flagellates was quantified using the concentrations of Chl-*a*. Detailed information on the physical module and coupled model has already been given in the previous studies (Guo et al., 2006; Wang et al., 2008; Wang et al., 2019; Zhao & Guo, 2011). The horizontal resolution of the model was $1/18^\circ$ (~ 6 km), and there were 21 terrain-following sigma layers in the vertical direction.

The model domain is 117.5–131.5°E, 24.0–41.0°N, which covered the Bohai Sea, Yellow Sea, and ECS (Fig. 1a). The Zhejiang coastal (ZC) region is defined as the enclosed area surrounded by three open boundaries and the coastline of Zhejiang Province (Fig. 1b). Sections N27 and N30 are the southern and northern open boundaries, which are located along the latitudes of 27°N and 30°N, respectively. Section B60 is set as the 60-m isobath, separating the ZC region from the outer sea. The endpoints of the three sections are denoted as A, B, C, and D. The cross-shelf section M extends from (121.5°E, 28.5°N) to (122.5°E, 27.5°N). According to previous studies on water exchange, the Kuroshio intrudes into the continental ECS through the 200-m isobath from the area northeast of Taiwan Island (Li et al., 2013; Liu et al., 2014; Zhang et al., 2019; Zhou et al., 2015). Therefore, in this study, the southwestern part of the 200-m isobath is defined as section B200 (Fig. 1b). The flux of nutrients through B200 was calculated to evaluate the effects of KI.

2.2 Model configurations

The model results of the climatologically seasonal variations in the physical and biochemical variables of the ECS have been validated and analyzed by Wang et al. (2019). In this study, the climatological results on 1 January from Wang et al. (2019) were used as the initial conditions. The model was integrated for 3 years, driven by the forcings of 2010, and then integrated continuously for 9 years, from 1 January 2010 to 31 December 2018. The model results from 2010 to 2018 were used to analyze the interannual variations.

Atmospheric forcing data from 2010 to 2018, including wind stress, sea surface pressure, surface net heat fluxes, evaporation, and precipitation, were derived from the ERA-interim reanalysis dataset of the European Center for Medium-Range Weather Forecasts (ECMWF; Dee et al., 2011). The data with a spatial resolution of 1/8° were interpolated to model grids. The model was driven by the 6-hourly wind stress data and the daily means of other atmospheric fluxes. The monthly runoff of the Changjiang River from 2010 to 2018 was obtained from the China River and Sediment Bulletin. The riverine DIN and DIP concentrations of the Changjiang River were set as constants (118.4 mmol/m³ for DIN, 1.3 mmol/m³ for DIP) according to observations in 2014 by Liang & Xian (2018). The physical open boundary conditions from 2010 to 2018, including the monthly means of the sea level, water temperature, salinity, and velocity, were obtained from the results of an assimilative model of the Japan Coastal Ocean Predictability Experiment (JCOPE2; Miyazawa et al., 2009). The other forcing data were set to be the same as those of Wang et al. (2019), therefore, they did not have interannual variations. These forcing data included (1) the nutrients from atmospheric deposition; (2) the freshwater runoff and riverine nutrient concentrations from rivers except for the Changjiang River; (3) the monthly concentrations of suspended particulate matter in the water; and (4) the nutrient concentrations and tidal constituents along the open boundary.

To quantitatively investigate the effects of the atmospheric forcing, river runoff from the Changjiang River, and KI on the nutrient supply and Chl-*a* concentration in the ZC region, four numerical experiments were carried out for the reference years 2013 and 2018. The details of

each numerical experiment are listed in Table 1. The 2018 simulation was set as the CONTROL run. The wind stress and other atmospheric conditions, including evaporation, precipitation, sea level pressure, and air-sea heat flux, were changed to those of 2013 in the experiments labeled as WIND and OTHERS, respectively. In the KURO experiment, the southern open boundary conditions were changed to those of 2013 to represent the change of KI northeast of Taiwan. In the RIVER experiment, the Changjiang River runoff was changed to that of 2013.

Table 1

Forcing conditions for the numerical experiments.

Experiment	Wind stress	Other atmospheric forcings except for wind stress	Southern open boundary conditions	Changjiang River runoff
WIND	2013	2018	2018	2018
OTHERS	2018	2013	2018	2018
KURO	2018	2018	2013	2018
RIVER	2018	2018	2018	2013

2.3 Observations

The daily SST data from 2010 to 2018 are acquired from the Operational Sea Surface Temperature and Sea Ice Analysis (OSTIA) system (Donlon et al., 2012). The spatial resolution of this SST data is $1/20^\circ$. In addition, the hourly satellite surface Chl-*a* concentrations were obtained from the Geostationary Ocean Color Imager (GOCI) provided by Korea Ocean Satellite Center (Ryu et al., 2012). The spatial resolution of this Chl-*a* data is 500 m. The satellite-derived SST and surface Chl-*a* concentrations are used to validate the modeled results.

In this study, samples for nutrient analysis were collected by R/V *haili* at 57 stations in the coastal areas of the ECS in the summer (5 to 19 August) of 2018 (Fig. 1a). The concentrations of DIN and DIP (unpublished data) were measured using a continuous-flow analyzer (AutoAnalyzer 3, Seal Analytical Ltd., UK) (SEAL Analytical Ltd., UK) (Zhao et al., 2018). Besides, the nutrient concentrations in August of 2013 derived from Yu (2014), and the DIN concentrations in July of 2018 derived from Lyu et al. (2020) are also collected (Fig. 1a) to validate the model results in summer when the ZCU prevails.

3 Results

3.1 Developing processes of the ZCU

The ZCU occurs in summer when the southwest summer monsoon prevails along the coastline of the ECS. The distributions of the 9-year average SST from late spring to early autumn indicate the developing processes of the ZCU (Fig. 2). In June (Fig. 2a), the SST decreased from south to north owing to the meridional variations in solar radiation. Cold water with a temperature lower

than 26 °C extended southward along the coastline of Zhejiang Province. The SST decreased from the open sea to the coast. In July (Fig. 2b), SST became warmer than that in June. The warm water extended northwestward from the open sea to the coastal areas. The 28 °C isotherm reached north to the latitude of 30°N. Near the coast of Zhejiang Province from the latitude of 28°N to 31°N, there was an isolated cold-water band enclosed by the 26 °C isotherm, which is thought to be the evidence of the formation of the ZCU. In August (Fig. 2c), the SST was high and became comparably uniform throughout the ECS owing to the strong solar radiation. The cold-water band enclosed by the 28°C isotherm could still be noticed near the coast of Zhejiang Province, but was not as obvious as that in July. Until early autumn (Fig. 2d), the SST increased southward and seaward. The isolated cold-water band caused by the ZCU tended to disappear.

Section M lies across the cold-water band near the coast (Fig. 2b, 2c). The vertical structures of the water temperature along section M from late spring to early autumn also indicate the developing processes of the ZCU. The isotherms tilted upward near the coastal area, indicating the occurrence of upwelling. In June (Fig. 2e), the 20 °C isotherm reached a depth of 30 m in the nearshore area but remained much deeper (about 50 m) in the offshore area. In July (Fig. 2f), the water was well-mixed in the nearshore area shallower than 15 m. Next to the well-mixed area was the cold-water band. The 20 °C isotherm reached up to a depth of 20 m, which was shallower than that in June, indicating more intense upwelling. In the offshore area, the water column was well-stratified. Until August (Fig. 2g), although the cold-water band at the sea surface was not as obvious as that in July due to the strengthened solar radiation (Fig. 2c), the upwelling in the nearshore area was still robust, as indicated by the upward-tilted isotherms. In September (Fig. 2h), upwelling disappeared, as indicated by the horizontally extended isotherms.

The modeled SST and vertical structures of temperature suggest that the ZCU starts to appear in June, strengthens in July and August, and then attenuates in September. The cold-water band at the sea surface is most obvious in July, therefore the SST distributions in July are used to analyze the interannual variations in the ZCU intensity.

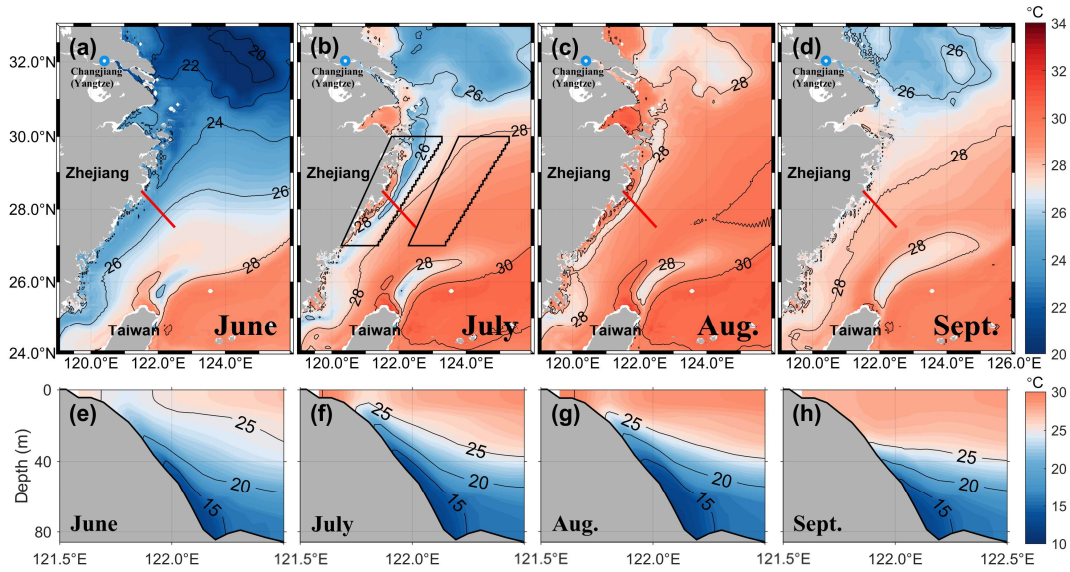


Figure 2. The modeled climatological (2010–2018) temperature. (a–d) SST and (e–h) the vertical structures of temperature along section M from June to September. Section M is noted by the thick red line in (a–d). The ZC region and EZC region are noted by the thick black line in (b).

3.2 Interannual variations in ZCU intensity

Upwelling pumps deep cold water up to the sea surface, forms a cold-water band, and increases the SST difference between the upwelling region and surrounding areas. Therefore, the zonal difference in SST between the upwelling region and the adjacent region is typically used to quantify the intensity of an upwelling (Jayaram et al., 2010; Lahiri & Vissa, 2022; Xu et al., 2017). In this study, the zonal SST difference (UI_{SST}) is defined as:

$$UI_{SST} = SST_{EZC} - SST_{ZC}$$

where SST_{ZC} is the mean SST of the ZC region, and SST_{EZC} is the mean SST of the East ZC (EZC) region, which is defined by shifting the ZC region eastward by 2° (Fig. 1b). A larger UI_{SST} indicates a stronger ZCU. The mean vertical velocity (w) in the entire ZC region is regarded as an explicit index of the ZCU intensity. In this study, both the UI_{SST} and w were used to define the strong and weak years of the ZCU.

The modeled SST averaged in the ZC region was compared with the satellite-derived SST from OSTIA for July from 2010 to 2018 (Fig. 3). The year-by-year variations of these two time series in July were consistent with a correlation coefficient of 0.87, which suggests that the model was able to reproduce the interannual variations in SST in the ZC region. The modeled interannual variations of SST in the ZC region were obvious, with a maximum value of 28.4 °C in 2018 and a minimum value of 25.8 °C in 2013. SST in the ZC region presented an obvious increasing trend from 2015 to 2018 and fluctuated from 2010 to 2014.

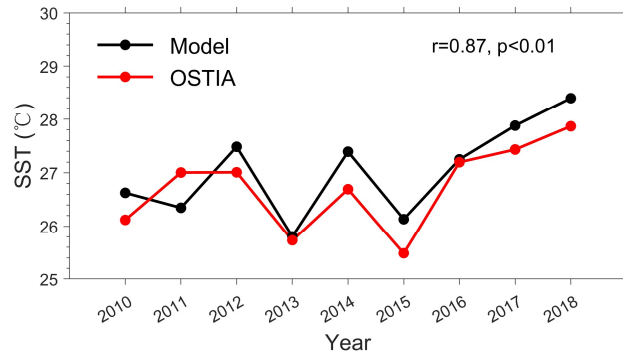


Figure 3. The model (black) and OSTIA (red) regionally averaged SST for July from 2010 to 2018. The averaged area is the ZC region denoted in Fig. 1b.

The differences in SST between the EZC and ZC regions (UI_{SST}) are shown in Fig. 4. The average SST in the EZC region was much higher than that in the ZC region (Fig. 2b), thus the UI_{SST} was positive in July for all the simulated years. The average value of UI_{SST} was 2.0 °C from 2010 to 2018, with a maximum value of 2.8 °C in 2011, and a minimum value of approximately 1.2 °C in 2014 and 2018. The larger the UI_{SST} , the stronger the upwelling. The UI_{SST} in 2011, 2013, and 2017 was much higher, exceeding one standard deviation during the nine years. The ZCU was weak in 2014 and 2018, as indicated by the lower UI_{SST} .

The interannual variations in w , which was averaged vertical velocity in the ZC region in July, are shown in Fig. 4 for a comparison with those of the UI_{SST} . The two variables exhibited similar interannual variations with a correlation coefficient of 0.80 (Fig. 4). Therefore, both the UI_{SST} and w gave the same result when they were used to define the strong and weak years of the ZCU. In the following analyses, 2013 was chosen to represent the strong ZCU year, when UI_{SST} was high and w was the strongest among the nine years. Between 2014 and 2018, we chose 2018 to represent the weak ZCU year. The reason for this choice is that there were intensive cruise observations in the coastal areas of the ECS in the summer of 2018, and the observed DIN and DIP concentrations can be used to validate the model results.

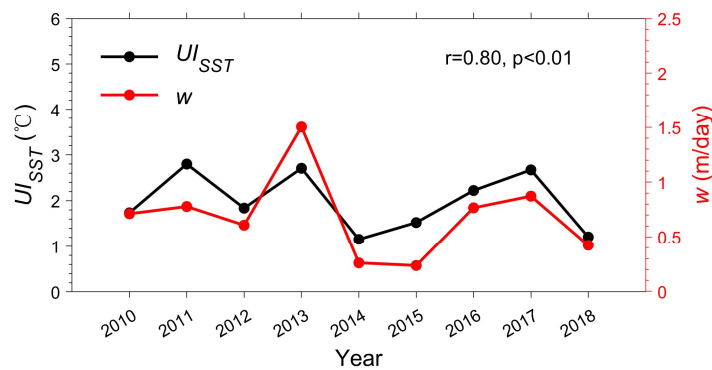


Figure 4. Time series of UI_{SST} (black) and w (red) for July from 2010 to 2018. UI_{SST} is the zonal SST difference between the EZC and ZC regions. w is the vertical velocity averaged in the entire ZC region.

3.3 Comparisons of temperatures and vertical velocities in the strong and weak ZCU years

The modeled SST in 2013 and 2018 were both characterized by low SST along the coast of Zhejiang Province in the summer (Fig. 5a, 5b), which indicated the occurrence of ZCU. Comparing the SST in these two years, it was obvious that the cold-water band was much more intense in 2013 than in 2018. The average SST in the ZC region was 25.8 °C in 2013 and 28.4 °C in 2018. Meanwhile, the UI_{SST} was 2.7 °C and 1.2 °C in 2013 and 2018, respectively. The larger UI_{SST} indicates a stronger ZCU in 2013 than in 2018.

The vertical structures of water temperature along section M also showed obvious differences caused by the different intensities of ZCU (Fig. 5c, 5d). The isotherms were located at a shallower place in 2013 than in 2018. Taking the 25 °C isotherm as an example, it reached the sea surface of the coastal area in 2013 but remained at a depth of approximately 10 m in 2018.

The average vertical velocity along section M was 1.11 m/day in 2013, which was approximately 4.5 times the value in 2018 (Fig. 5e, 5f). The upward vertical velocities appeared from near the coast to a longitude of 122.2°E along section M. The upward velocities occupied a larger area along section M in 2013 than in 2018. The maximum upward vertical velocity was 9.1 m/day occurring at the bottom of the longitude of 122.0°E in 2013, but it was only 5.1 m/day in 2018.

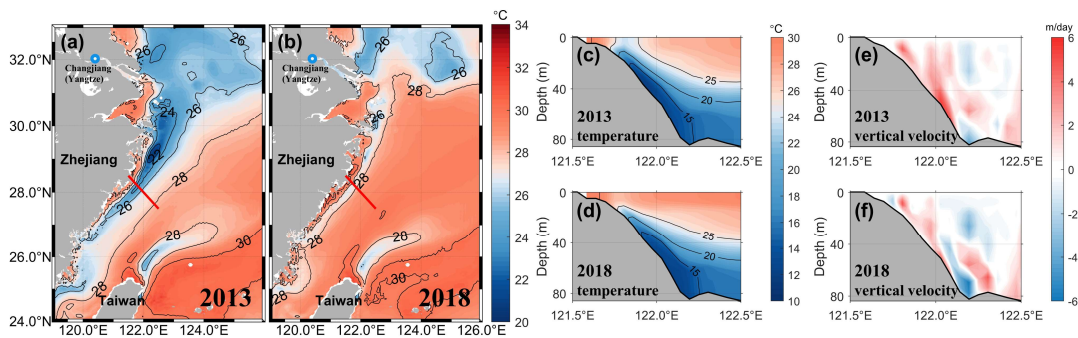


Figure 5. Comparisons of (a, b) SST, vertical distribution of (c, d) water temperature and (e, f) vertical velocity along section M in July of the strong (2013) and the weak (2018) ZCU years. Section M is noted by thick red line in (a, b). Positive values of the vertical velocity in (e, f) represent upward one.

3.4 Comparisons of nutrient concentrations in the strong and weak ZCU years

The climatologically seasonal variations in nutrient concentrations in the ECS have already been validated in previous studies (Wang et al., 2019; Zhang et al., 2019). In this study, intensive observations of nutrient concentrations in the coastal areas of the ECS in the summer of 2013 and 2018 overlapped with the modeled distributions (Fig. 6, 7). The agreement between the observations and model results suggest that the model successfully reproduced the distributions of nutrient concentrations in summer when the ZCU occurred.

The concentrations of DIN and DIP at the sea surface and bottom in 2013 and 2018 were compared to quantify the influence of the ZCU on nutrient supply. At the surface, the distributions of DIN concentrations in both 2013 and 2018 were similar (Fig. 6a, 6b). The area with a concentration greater than 50 mmol/m³ appeared near the Changjiang Estuary (Fig. 1b) and extended northeastward along with the extension of the Changjiang diluted water, which was also validated by observations. This indicated that the Changjiang River is an important source of DIN for the northern ECS. DIN concentrations were high along the coastline of Zhejiang Province within the 60-m isobath, and decreased sharply seaward. The concentrations remained low (less than 1 mmol/m³) in areas with depths greater than 60 m. To probe the interannual variations in DIN concentrations, the differences in DIN concentrations between 2013 and 2018 were calculated (Fig. 6c). In the ZC region, DIN concentrations were much higher in the strong upwelling year (2013), as indicated by the positive differences. Positive DIN differences were also found in the Changjiang Estuary and its northeastward area. The Changjiang runoff was 2.7×10^{11} m³ from April to June 2013, which was larger than that in 2018 (2.2×10^{11} m³). Greater amounts of river input in 2013 induced higher DIN concentrations near the Changjiang Estuary. Moreover, the stronger southwest monsoon in 2013 contributed to the northeastward extension of N-rich river water.

The modeled concentrations of DIP were low throughout the entire ECS at the surface (Fig. 6d, 6e), during the summers of both 2013 and 2018. This is because DIP acts as the limiting nutrient in the ECS, and was nearly used up by phytoplankton growth. The DIP concentrations had comparably high values (over 0.2 mmol/m³) in coastal regions, and then decreased seaward, as indicated by both model results and observations. In 2018, scattered high DIP concentrations (over 0.6 mmol/m³) appeared near the Changjiang Estuary and Hangzhou Bay (Fig. 1b), which were caused by the episodic supply contributed by the Changjiang River, but they were not captured by the model. In the ZC region, there was an area with weak positive differences in DIP concentrations (Fig. 6f), whose position was consistent with that of the cold-water band induced by the ZCU (Fig. 5a). However, the interannual variations in the DIP concentrations were not as obvious as those of the DIN (Fig. 6c). Because DIP was the limiting nutrient, the standing stocks did not reflect the amount supplied by the ZCU. In contrast to the DIN, the differences in DIP concentrations were negative near the Changjiang Estuary, indicating that the DIP concentration in the ECS was not determined solely by Changjiang River runoff. Biological processes played a more important role in the distribution of DIP concentrations.

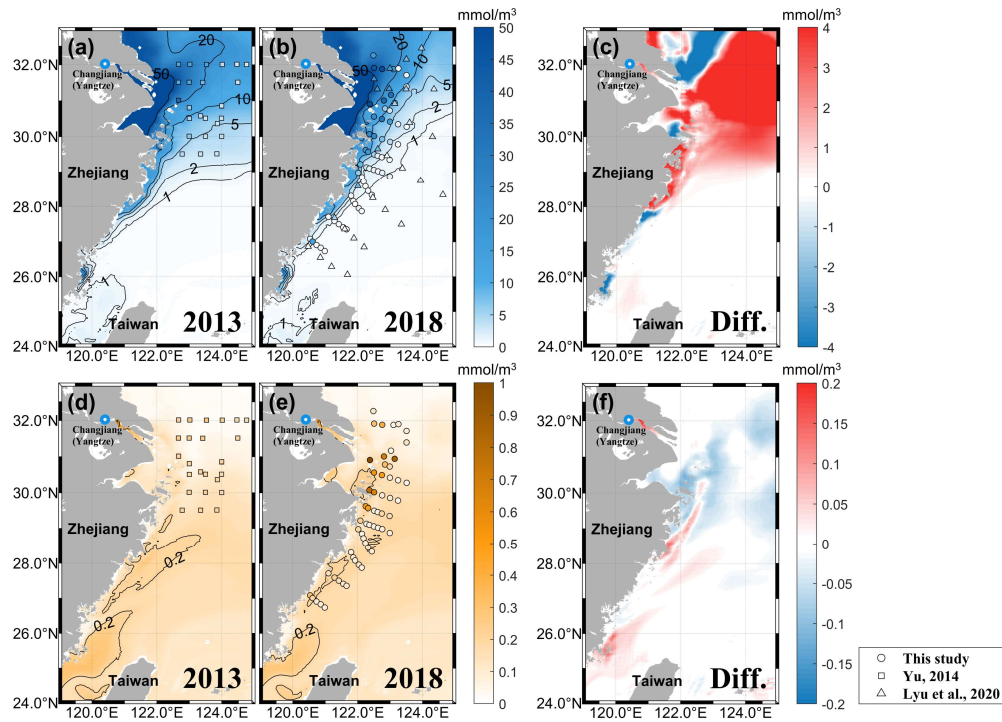


Figure 6. Comparisons of (a, b) DIN and (d, e) DIP concentrations at the sea surface in July of the strong (2013) and the weak (2018) ZCU years, and (c, f) differences between these two years. The contour plot represents model results while the colored dots represent in situ observations in the summer of 2013 and 2018.

At the bottom, the highest DIN concentrations also appeared near the Changjiang Estuary in both 2013 and 2018 (Fig. 7a, 7b). The DIN concentrations were much higher at the bottom than at the surface on the continental shelf of the ECS. A higher DIN concentration band (over 5 mmol/m³), originating from the shelf break northeast of Taiwan Island, passed through the 200-m isobath (section B200 in Fig. 7), extended northwestward to the coast, and then turned northeastward along the coastline to the Changjiang Estuary. The location of the band was consistent with the intrusion path of NKBC in the ECS, which is known to deliver the nutrients from KI (Yang et al., 2011, 2013). The differences in DIN concentrations were positive within the nearshore area, but negative in the wide deeper areas of the continental shelf (Fig. 7c).

The DIP concentrations at the bottom (Fig. 7d, 7e) were significantly higher than those at the surface (Fig. 6d, 6e), which agreed well with the observations. The concentrations in the coastal areas were over 0.6 mmol/m³ and remained at high values of 0.4 mmol/m³ out of the 60-m isobath. The path of NKBC was also indicated by the extension of the band with higher DIP concentrations (over 0.6 mmol/m³). Therefore, KI can be regarded as a critical source of nutrients to the bottom of the ZC region in summer, especially for DIP (Xu et al., 2020; Yang et al., 2013). In nearshore areas, there were positive DIP differences, indicating higher DIP concentrations in 2013 with a stronger ZCU (Fig. 7f). The much wider areas of the ECS were

dominated by negative differences at the bottom. The differences in DIN and DIP concentrations between 2013 and 2018 exhibited similar distributions at the bottom (Fig. 7c, 7f).

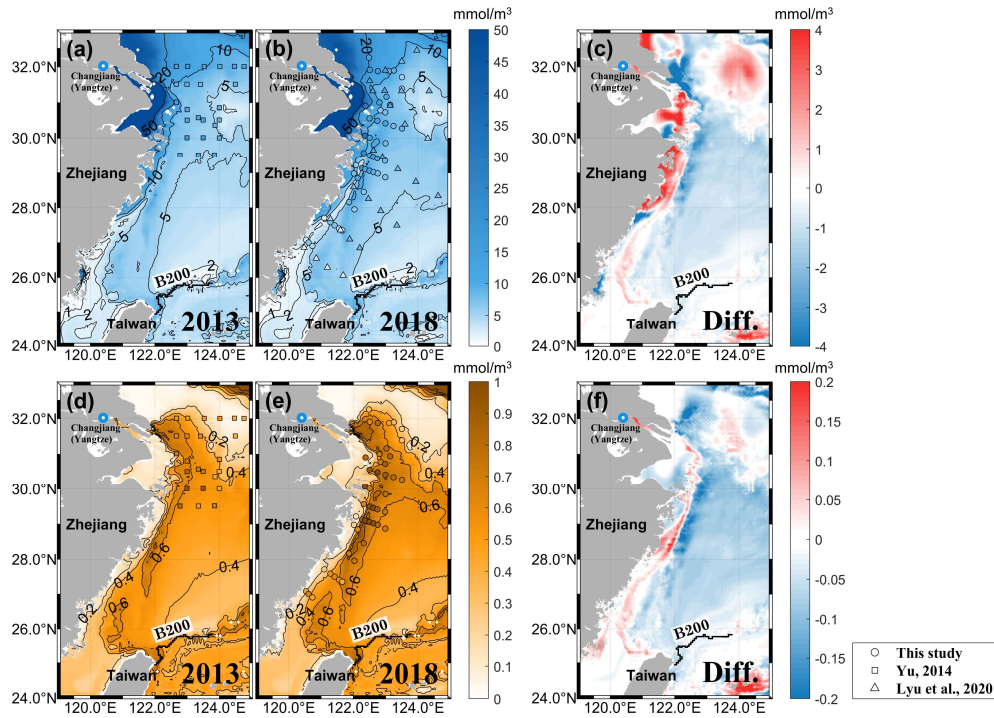


Figure 7. Same as Figure 6, but for the nutrients at the sea bottom. The sea bottom is defined as the deepest sigma-layer in the model that is 97.5% of the total water depth. For the grids deeper than 200m, the data are replaced by the data at 200m depth. Section B200 is noted by the thick black line.

3.5 Comparisons of the phytoplankton biomass in the strong and weak ZCU years

In summer, the surface phytoplankton biomass was much higher in the Changjiang Estuary and the adjacent ZC region, with Chl-*a* concentrations higher than 2 mg/m^3 , as indicated by both the model results and satellite observations from GOCI for these two years (Fig. 8a, 8b, 8d and 8e). The high surface Chl-*a* concentrations in the Changjiang Estuary were supported by the large input of nutrients from the Changjiang River, whereas the high values along the coast of Zhejiang Province were attributed to the supply of nutrients due to the ZCU. Comparing the situations in 2013 and 2018, the modeled differences in Chl-*a* concentrations were positive in the ZC region (Fig. 8c). The distributions of satellite-derived differences were patchier and not as uniform as the model results (Fig. 8f). However, they both suggested that Chl-*a* concentrations were higher in the ZC region in 2013. In the deeper continental shelf region, there were no obvious differences in the Chl-*a* concentrations between these two years.

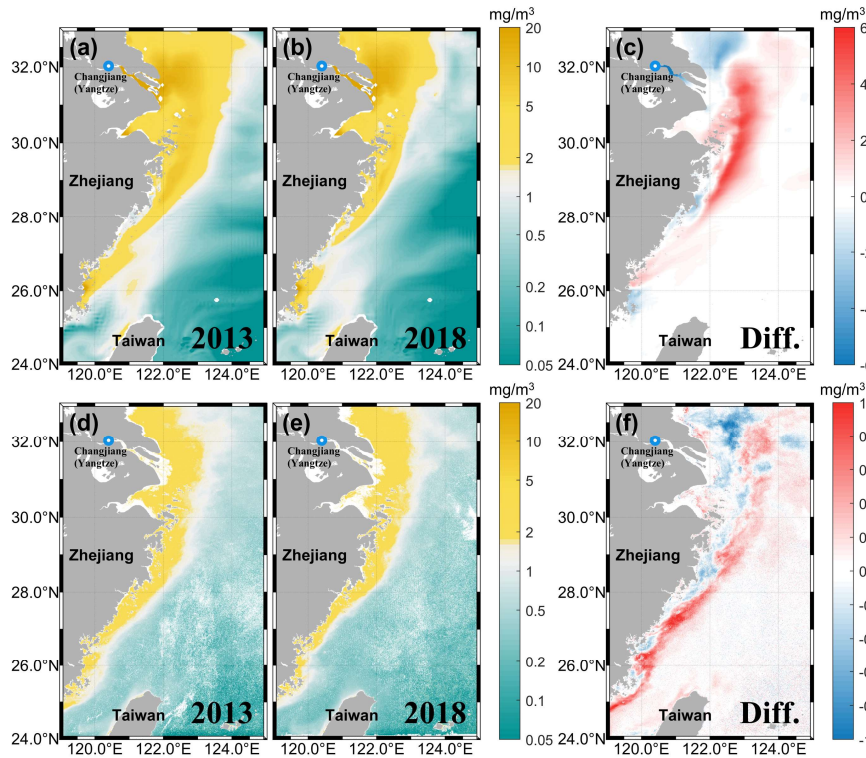


Figure 8. Comparisons of (a, b) modeled and (d, e) GOCI sea surface Chl-*a* concentrations in July of the strong (2013) and weak (2018) ZCU years, and (c, f) differences between these two years.

4 Discussion

4.1 The nutrient transports of the ZCU and KI

The ZC region is surrounded by three open boundaries (N27, B60, and N30) and the coastline (Fig. 1b). The fluxes of DIN and DIP through these three open boundaries in July 2013 and 2018 were calculated to interpret the nutrient budget of the ZC region (Fig. 9). In July 2013 and 2018, nutrients were transported into the ZC region through the southern boundary (N27) for both DIN and DIP, and were transported out of the region through the northern boundary (N30). The northeastward currents along the coastline, induced by the summer monsoon (Gan et al., 2016), were responsible for the transport of nutrients across N27 and N30. However, the distribution of nutrient fluxes at B60 was much more complicated. Shoreward transport dominated the lower water layers (deeper than 20 m), which was induced by the ZCU going up along the sea bottom. Meanwhile, seaward transport occupied the upper layers, which was the effect of offshore Ekman transport induced by alongshore wind stress.

The nutrient fluxes at these three open boundaries exhibited clear differences between 2013 and 2018 (Fig. 9). Taking DIP as an example (Fig. 9c, 9d; Table 2), the amounts of DIP transported into the ZC region across N27 were 4.54×10^8 mol and 3.24×10^8 mol in July 2013 and 2018,

respectively. During the same period, the DIP fluxes across N30 were -2.88×10^8 mol in 2013 and -1.95×10^8 mol in 2018. Negative values indicate the export of DIP at N30. The transport amounts were much larger in 2013 than those in 2018 for both imports at N27 and exports at N30, which was attributed to the stronger alongshore currents in 2013. The distributions of DIP fluxes at B60 were similar in 2013 and 2018, with seaward transport in the upper 20 m, and shoreward transport in the deeper water layers; nevertheless, the fluxes in 2013 were much more intense. At deeper layers of B60 (20–60 m), 4.23×10^8 mol of DIP was transported into the ZC region by the ZCU in July 2013, which was about 10 times the value in 2018 (0.40×10^8 mol). This indicated greater transport by the stronger ZCU in 2013. The net flux over the entire B60 was 1.40×10^8 mol in July 2013. However, the value was -0.83×10^8 mol in 2018. At B60, the net inflow in 2013 and net outflow in 2018 resulted in positive differences in DIP concentrations in the nearshore areas (Fig. 6f, 7f). The net DIP flux through these three open boundaries was 3.06×10^8 mol in July 2013, which was approximately six times that of 2018 (0.46×10^8 mol). DIP acted as a limiting nutrient in the ZC region. More DIP supplies in 2013 promoted biogeochemical cycles of N and P in the seawater. Taking the variations in DIP as an example, the net contributions of biological processes, including photosynthesis, respiration, mineralization, and benthic release was -2.45×10^8 mol in July 2013, but only -0.38×10^8 mol in July 2018. The greater absorption of DIP resulted in higher Chl-*a* concentrations in the ZC region in 2013 (Fig. 8c).

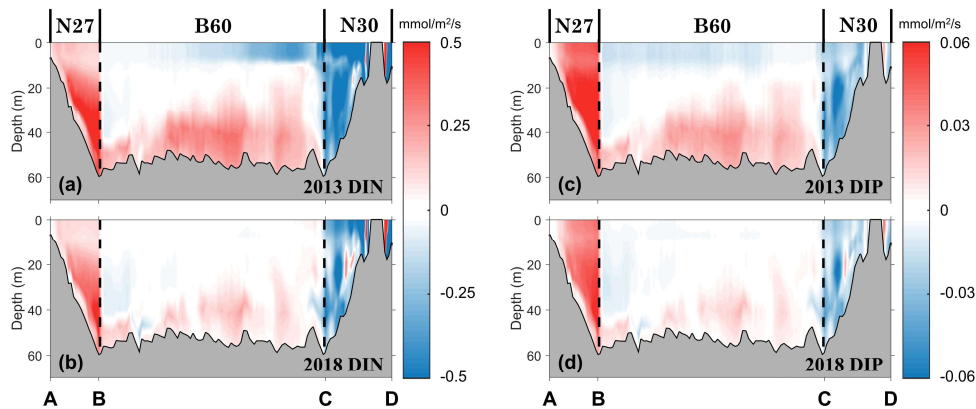


Figure 9. Spatial distributions of (a, b) DIN and (c, d) DIP fluxes along the three open boundaries of the ZC region (N27, B60 and N30, see Fig. 1b) in July of the strong (2013) and weak (2018) ZCU years. Positive values represent the flux into the ZC region. The flux at B60 was horizontally 5-points running mean. The A, B, C, and D represent the endpoints of the sections.

KI is regarded as an important source of nutrients in the ECS, especially for DIP (Lin et al., 2019; Yang et al., 2013). The amounts of nutrients transported across B200 between 2013 and 2018 were compared to evaluate the effects of KI. Given that there is a time lag between the occurrence of the KI at B200 and its effect in the coastal areas, Xu et al. (2020) used a group of numerical experiments to point out that the nutrients from the KI integrated from March to June influenced the growth of phytoplankton in July in the coastal areas of the ECS. Based on the

results of our model, 1.21×10^{11} mol DIN and 1.63×10^{10} mol DIP were transported to the continental ECS across B200 from March to June in 2013, whereas in 2018 the values were 1.64×10^{11} mol DIN and 2.10×10^{10} mol DIP. It was apparent that the supplies from KI in 2013 were less than those in 2018, which was the reason for the negative differences in DIN and DIP concentrations at the bottom of the wide continental ECS between 2013 and 2018 (Fig. 7c, 7f).

4.2 The key factors determining nutrient supply in the ZC region

There were obvious differences in the nutrient supply, nutrient standing stocks, and Chl-*a* concentrations between 2013 and 2018. To probe the key factors determining these differences, a group of numerical experiments were carried out as described in Table 1.

In WIND, the wind stress was changed to that of 2013, and the other conditions were the same as those in 2018 (CONTROL). The ZCU intensity in WIND varied significantly compared with that in 2018 (Table 2). The simulated average w in the ZC region was 1.46 m/day, which was approximately three times the value in 2018 (0.42 m/day). Comparing the results of WIND and 2013, the same stronger wind stress induced the stronger upwelling, as indicated by the similar w . Therefore, wind stress was an important factor in deciding the ZCU intensity. The amount of DIP supplied by KI from March to June was 2.04×10^{10} mol in WIND, which was similar to the value of 2.10×10^{10} mol in 2018, but larger than the value of 1.63×10^{10} mol in 2013. Therefore, wind stress did not have a significant influence on the nutrient supply by KI. In the ZC region, the DIP fluxes through N27 and N30 were larger in WIND than in 2018, and a stronger ZCU also transported more DIP across B60 into the ZC region. Therefore, the local alongshore wind in the summer determined the ZCU intensity and played an important role in establishing the nutrient supply of coastal regions. As a result, a greater nutrient supply in the ZC region supported the growth of phytoplankton, which was reflected in the higher Chl-*a* concentrations of 2.06 mg/m^3 in WIND and 1.85 mg/m^3 in 2013 than the value of 1.34 mg/m^3 in 2018.

In KURO, the southern open boundary conditions of the model were changed to those of 2013. The amount of DIP supplied by KI from March to June in KURO (1.58×10^{10} mol) was smaller than that in 2018 (2.10×10^{10} mol) but was similar to that in 2013 (1.64×10^{10} mol). Therefore, the southern open boundary conditions determined the nutrients supplied by KI to the continental ECS. However, with the same weaker alongshore wind stress in KURO and in 2018, the ZCU intensity and DIP fluxes at the three open boundaries of the ZC region were similar (Table 2). This suggests that the different amounts of nutrients supplied by KI between 2013 and 2018 did not significantly influence the nutrient budget of the ZC region. As a result, the Chl-*a* concentration in the ZC region in KURO was as low as that in 2018.

The results of the experiments OTHERS and RIVER were similar to those of 2018 (not shown in Table 2). This suggests that the other atmospheric forcings except wind stress did not influence the nutrient supply or phytoplankton biomass in the ZC region. The Changjiang diluted water extended northeastward, driven by the southwest summer monsoon. Therefore, nutrients from the Changjiang River tend to influence the areas north of the ZC region. Previous studies have

also noted that the input from the Changjiang River does not influence the phytoplankton biomass in the coastal areas of Zhejiang Province (Xu et al., 2020).

Table 2

Comparisons among the cases 2013, WIND, KURO and CONTROL (2018) in July in the ZC region

Case	ZCU intensity (m/day)	DIP flux (10^8 mol)			Chl- <i>a</i> concentration (mg/m ³)
		N27	B60	N30	
2013	1.51	4.54	1.40	-2.88	1.85
WIND	1.46	4.93	1.55	-3.02	2.06
KURO	0.41	2.98	-0.62	-1.86	1.31
CONTROL (2018)	0.42	3.24	-0.83	-1.95	1.34

Note. The ZCU intensity is quantified as the average vertical velocity in the ZC region.

To identify the main areas where the ZCU and KI distribute DIP, the results of WIND and KURO were compared with those of 2018. Figure 10 shows the differences in DIP concentrations in WIND and KURO minus those in CONTROL (2018) at the surface and bottom. In WIND (Fig. 10a, 10b), the positive differences dominated the coastal areas of Zhejiang Province at both the surface and bottom, which is consistent with the shoreward nutrient supply induced by the stronger ZCU in WIND (Table 2). The differences in the DIP concentrations between 2013 and 2018 in the nearshore areas (Fig. 6f, 7f) can also be attributed to the effects of the ZCU. However, the negative differences in DIP concentration between 2013 and 2018 dominated the bottom of the wide continental areas (Fig. 7f), which cannot be explained by the results of WIND (Fig. 10b). The weaker KI was the main influencing factor, as indicated by the similar distribution of negative DIP differences at the bottom in 2013 (Fig. 7f) and in KURO (Fig. 10d). However, the KI did not have an obvious influence on the DIP concentrations at the surface (Fig. 10c).

The nutrient supply revealed by the numerical experiments indicated that KI intensity determined the nutrient concentrations at the bottom of the ECS. The amount of these nutrients transported to the surface in the ZC region depended on the intensity of the wind-induced ZCU.

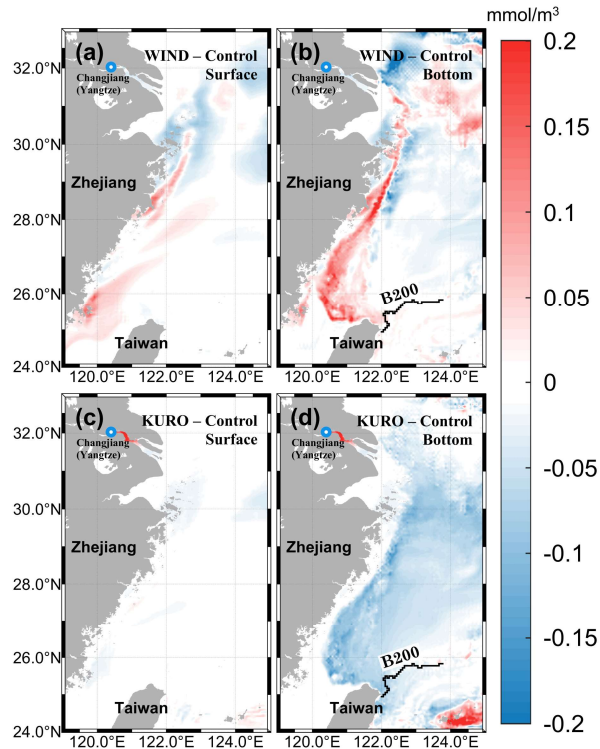


Figure 10. The differences in DIP concentrations between numerical experiments and CONTROL (2018). The differences between WIND and CONTROL at (a) surface and (b) bottom. The differences between KURO and CONTROL at (c) surface and (d) bottom. For the grids deeper than 200 m, the data are replaced by the data at 200 m depth. Section B200 is noted by the thick black line.

4.3 The effects of the ZCU and KI on phytoplankton biomass

To investigate the response of phytoplankton biomass to nutrient supply, the vertical structures of the Chl-*a* concentrations, averaged in the ZC and EZC regions (Fig. 1b) in July, were analyzed for cases 2013, WIND, KURO, and 2018 (Fig. 11).

The vertical structures of the Chl-*a* concentrations in the ZC and EZC regions were significantly different in summer. In the ZC region, the Chl-*a* concentrations remained higher (over 2.0 mg/m³) in the upper water layers that were shallower than 10 m, and then decreased with increasing water depth (Fig. 11a). At a depth of 30 m, the Chl-*a* concentration decreased to approximately zero. These modeled vertical characteristics were consistent with the nearshore in situ observations in Fig. 11a (Chen et al., 2021; Wei et al., 2021). In the offshore EZC region, the water was well-stratified in summer, and nutrients were depleted by phytoplankton at the surface. Under the influence of both nutrients and light, the subsurface chlorophyll maximum formed. This phenomenon has been confirmed in many historical observations of the offshore areas of the ECS (Furuya et al., 2003; Lee et al., 2017; Xu et al., 2022). The modeled depth of

subsurface chlorophyll maximum was approximately 50 m, which was in the range of observed depths (20–50 m). The modeled maximum value ($2.0\text{--}3.0\text{ mg/m}^3$) was also in the range of observations ($1.0\text{--}3.0\text{ mg/m}^3$).

In WIND and 2013, more nutrients were pumped up by the stronger ZCU, which supported greater Chl-*a* concentrations ($\sim 4.0\text{ mg/m}^3$) at the sea surface in the ZC region (red and orange lines in Fig. 11a). The surface Chl-*a* concentrations in KURO and in 2018 (blue and black lines in Fig. 11a) were only half of those in WIND and in 2013, which were induced by a weaker ZCU. At the depth of 50 m in the EZC region, the maximum Chl-*a* concentrations in WIND and in 2018 reached about 3.0 mg/m^3 under the influence of stronger KI in these two cases (orange and black lines in Fig. 11b), whereas the concentrations were only approximately 2.0 mg/m^3 in KURO and in 2013, with weaker KI (red and blue lines in Fig. 11b). The comparison of these four cases indicated that the ZCU mainly determined the phytoplankton biomass in nearshore areas, whereas the KI mainly regulated the intensity of the subsurface chlorophyll maximum in the offshore areas. The intensity of the ZCU was similar in WIND and 2013. However, more nutrients supplied by the KI in WIND also resulted in higher Chl-*a* concentrations at the surface in the ZC region in WIND than those in 2013 (red and orange lines in Fig. 11a; Table 2).

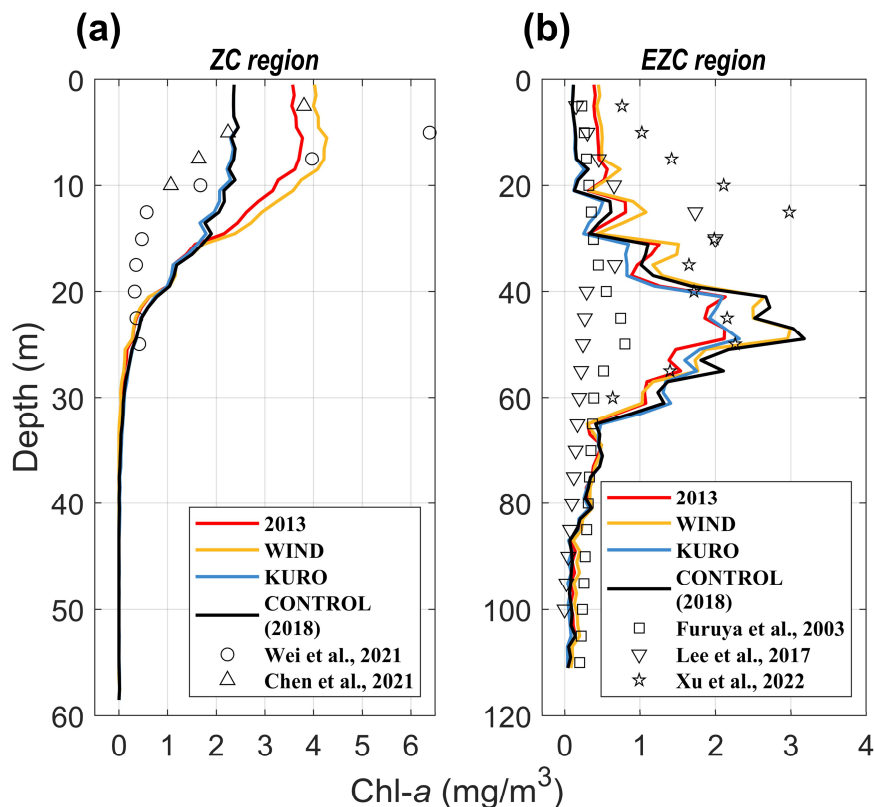


Figure 11. Vertical structures of Chl-*a* concentrations horizontally averaged in the (a) ZC and (b) EZC regions in July of the cases 2013, WIND, KURO, and CONTROL (2018). Scatters represent observed nearshore and offshore Chl-*a* concentration profiles in summer.

5 Conclusions

The ZCU prevails near the coastal area of the ECS in summer, and KI is regarded as an important oceanic source of DIP. The primary production is reported to be high in summer when the ZCU pumps up DIP oriented from the Kuroshio to the euphotic layers. However, the interannual variations in both ZCU and KI intensities are not consistent. Therefore, their contributions to the nutrient supplies may vary a lot.

In this study, a three-dimensional physical-biochemical model was applied to evaluate the influence of the ZCU and KI on the interannual variations of nutrient concentration and phytoplankton biomass. After validating the modeled SST with the satellite-derived data in the ZC region in 2010–2018 period, the years 2013 and 2018 were determined as the strong and the weak year of the ZCU, as indicated by both UI_{SST} and w . The surface DIP concentrations were lower than 0.30 mmol/m^3 in the two years. Comparing the results at the sea bottom in 2013 and 2018, the bottom DIP concentrations in 2013 were approximately 0.20 mmol/m^3 higher than in 2018 in nearshore areas, whereas were approximately 0.08 mmol/m^3 lower than in 2018 in offshore areas. The stronger ZCU in July 2013 induced net shoreward rather than seaward DIP transport at the 60-m isobath ($1.40 \times 10^8 \text{ mol}$ in 2013, $-0.83 \times 10^8 \text{ mol}$ in 2018), which resulted in higher nearshore DIP concentrations. The weaker KI in the spring (March–June) of 2013 decreased the amount of DIP supply from the open ocean ($1.63 \times 10^{10} \text{ mol}$ in 2013, $2.10 \times 10^{10} \text{ mol}$ in 2018), and resulted in lower offshore DIP concentrations. The greater nutrient supply in nearshore areas in 2013 significantly promoted primary production and increased phytoplankton biomass (1.85 mg/m^3 in 2013, 1.34 mg/m^3 in 2018).

Through a group of numerical experiments, the wind stress and the southern open boundary conditions were regarded as the key factors influencing the interannual variations of nutrient and Chl-*a* concentrations in the ECS. This is because wind stress decided the ZCU intensity, whereas the southern open boundary conditions represented the KI intensity. With similar KI intensities, the ZCU intensities between 2013 and 2018 determined the nutrient supply and concentrations of the ZC region within the 60-m isobath. The KI intensities influenced the nutrients supplied from B200 and the nutrient concentrations at the bottom of the wide ECS continental shelf. The subsurface chlorophyll maximum in the offshore ECS in summer was controlled by the KI intensity, while the nearshore phytoplankton biomass was mainly determined by the ZCU intensity.

The intensity of KI was weak in 2013 with a strong ZCU, while KI was strong in 2018 with a weak ZCU. The intensities of KI and ZCU happened to be inconsistent in these two years. In this study, the importance of the ZCU to coastal nutrient supply and phytoplankton biomass was highlighted. But the influence of KI on coastal areas (the ZC region) can also be noticed. For example, in cases 2013 and WIND, which have a similar intensity of ZCU, the net DIP flux through open boundaries of the ZC region was higher in WIND ($3.46 \times 10^8 \text{ mol}$) than in 2013 ($3.06 \times 10^8 \text{ mol}$), owing to the stronger KI in WIND. It should be noted that the effect of KI can be impeded by weaker ZCU. Because when the intensity of ZCU was weak in KURO and 2018,

the net DIP fluxes were 0.50×10^8 mol and 0.46×10^8 mol, respectively, which represented a slight difference. This result suggests that there exist nonlinear effects between the ZCU and KI to regulate coastal nutrient supply in the ECS.

Acknowledgments

This study was supported by the National Nature Science Foundation of China (NSFC) (42176022, U1806214, and 42076034). X. GUO was supported by a Grant-in-Aid for Scientific Research (MEXT KAKENHI, grant number: 20H04319, 22H05206).

Open Research

Data availability statement

The OSTIA SST data used in this study are the Reprocessed foundation SST analyses data available at <https://ghrsst-pp.metoffice.gov.uk/ostia-website/index.html>. The GOCI chlorophyll data are obtained from <http://kosc.kiost.ac.kr/gociSearch/list.nm?menuCd=50&lang=en&url=gociSearch>. The ERA-interim dataset is available at <https://apps.ecmwf.int/datasets/data/interim-full-daily/levtype=sfc>. The China River and Sediment Bulletin are available at <http://www.mwr.gov.cn/sj>. The JCOPE2 data are provided by Japan Agency for Marine-Earth Science and Technology (JAMSTEC, <http://www.jamstec.go.jp/jcope>).

The model results that support the findings of this study are available online at <https://data.mendeley.com/datasets/jm3h5mgn3n/draft?a=1aacb6b2-ba0d-4aac-aaec-0048a16488d9>

References

- 685 Albert, A., Echevin, V., Lévy, M., & Aumont, O. (2010). Impact of nearshore wind stress curl on
686 coastal circulation and primary productivity in the Peru upwelling system. *Journal of*
687 *Geophysical Research*, 115, C12. <https://doi.org/10.1029/2010JC006569>
- 688 Bakun, A. (1973), Coastal upwelling indices, west coast of North America, 1946–71, NOAA
689 Technical Report NMFS SSRF-671, U.S. Department of Commerce.
- 690 Barber, R. T., Marra, J., Bidigare, R. C., Codispoti, L. A., Halpern, D., Johnson, Z., et al. (2001).
691 Primary productivity and its regulation in the Arabian Sea during 1995. *Deep Sea Research Part*
692 *II: Topical Studies in Oceanography*, 48, 1127–1172. [https://doi.org/10.1016/S0967-](https://doi.org/10.1016/S0967-0645(00)00134-X)
693 [0645\(00\)00134-X](https://doi.org/10.1016/S0967-0645(00)00134-X)
- 694 Blumberg, A. F., & Mellor, G. L. (1987). A description of a three-dimensional coastal ocean
695 circulation model. *Three-dimensional coastal ocean models*, 4, 1–16.
696 <https://doi.org/10.1029/co004p0001>
- 697 Bograd, S. J., Schroeder, I., Sarkar, N., Qiu, X., Sydeman, W. J., & Schwing, F. B. (2009).
698 Phenology of coastal upwelling in the California Current. *Geophysical Research Letters*, 36,
699 L01602. <https://doi.org/10.1029/2008GL035933>
- 700 Capone, D., & Hutchins, D. (2013) Microbial biogeochemistry of coastal upwelling regimes in a
701 changing ocean. *Nature Geoscience*, 6, 711–717. <https://doi.org/10.1038/ngeo1916>
- 702 Chen, C.-C., Shiah, F.-K., Gong, G.-C., & Chen, T.-Y. (2021). Impact of upwelling on
703 phytoplankton blooms and hypoxia along the Chinese coast in the East China Sea. *Marine*
704 *Pollution Bulletin*, 167, 112288. <https://doi.org/10.1016/j.marpolbul.2021.112288>
- 705 Dee, D. P., Uppala, S. M., Simmons, A. J., Berrisford, P., Poli, P., Kobayashi, S., et al. (2011).
706 The ERA-Interim reanalysis: Configuration and performance of the data assimilation system.

Quarterly Journal of the Royal Meteorological Society, 137, 553–597.

<https://doi.org/10.1002/qj.828>

Donlon, C. J., Martin, M., Stark, J., Roberts-Jones, J., Fiedler, E., & Wimmer, W. (2012). The operational sea surface temperature and sea ice analysis (OSTIA) system. *Remote Sensing of Environment*, 116, 140–158. <https://doi.org/10.1016/j.rse.2010.10.017>

Furuya, K., Hayashi, M., Yabushita, Y., & Ishikawa, A. (2003). Phytoplankton dynamics in the East China Sea in spring and summer as revealed by HPLC-derived pigment signatures. *Deep Sea Research Part II: Topical Studies in Oceanography*, 50(2), 367–387.

[https://doi.org/10.1016/s0967-0645\(02\)00460-5](https://doi.org/10.1016/s0967-0645(02)00460-5)

Fang, G., Zhao, B., & Zhu, Y. (1991). Water volume transport through the Taiwan Strait and the continental shelf of the East China Sea measured with current meters. *Elsevier oceanography series*, 54, 345–358. [https://doi.org/10.1016/S0422-9894\(08\)70107-7](https://doi.org/10.1016/S0422-9894(08)70107-7)

Fréon, P., Barange, M., & Arístegui, J. (2009). Eastern boundary upwelling ecosystems: Integrative and comparative approaches. *Progress in Oceanography*, 83(1–4), 1–14.

<https://doi.org/10.1016/j.pocean.2009.08.001>

Gan, J., Liu, Z., & Liang, L. (2016). Numerical modeling of intrinsically and extrinsically forced seasonal circulation in the China Seas: A Kinematic Study. *Journal of Geophysical Research: Oceans*, 121(7), 4697–4715. <https://doi.org/10.1002/2016jc011800>

Guo, X., Miyazawa, Y., & Yamagata, T. (2006). The Kuroshio onshore intrusion along the shelf break of the East China Sea: The origin of the tsushima warm current. *Journal of Physical Oceanography*, 36(12), 2205–2231. <https://doi.org/10.1175/jpo2976.1>

- 728 Hahm, D., Rhee, T. S., Kim, H.-C., Jang, C. J., Kim, Y. S., & Park, J.-H. (2019). An observation
729 of primary production enhanced by coastal upwelling in the Southwest East/Japan sea. *Journal of*
730 *Marine Systems*, 195, 30–37. <https://doi.org/10.1016/j.jmarsys.2019.03.005>
- 731 Hu, B., Li, J., Zhao, J., Wei, H., Yin, X., Li, G., et al. (2014). Late Holocene elemental and
732 isotopic carbon and nitrogen records from the East China Sea inner shelf: Implications for
733 monsoon and upwelling. *Marine Chemistry*, 162, 60–70.
734 <https://doi.org/10.1016/j.marchem.2014.03.008>
- 735 Hu, J., & Wang, X. H. (2016). Progress on upwelling studies in the China seas. *Reviews of*
736 *Geophysics*, 54, 653–673. <https://doi.org/10.1002/2015RG000505>
- 737 Hu, Q., Chen, X., Huang, W., & Zhou, F. (2021). Phytoplankton bloom triggered by eddy-wind
738 interaction in the upwelling region east of Hainan Island. *Journal of Marine Systems*, 214,
739 103470. <https://doi.org/10.1016/j.jmarsys.2020.103470>
- 740 Jacox, M. G., Bograd, S. J., Hazen, E. L., & Fiechter, J. (2015). Sensitivity of the California
741 current nutrient supply to wind, heat, and remote ocean forcing. *Geophysical Research Letters*,
742 42(14), 5950–5957. <https://doi.org/10.1002/2015gl065147>
- 743 Jayaram, C., Chacko, N., Joseph, K. A., & Balchand, A. N. (2010). Interannual variability of
744 upwelling indices in the southeastern Arabian Sea: A satellite based study. *Ocean Science*
745 *Journal*, 45(1), 27–40. <https://doi.org/10.1007/s12601-010-0003-6>
- 746 Jing, Z., Qi, Y., & Du, Y. (2011). Upwelling in the continental shelf of northern South China Sea
747 associated with 1997–1998 El Niño. *Journal of Geophysical Research*, 116(C2), C02033.
748 <https://doi.org/10.1029/2010JC006598>

- Lahiri, S. P., & Vissa, N. K. (2022). Assessment of Indian Ocean upwelling changes and its relationship with the Indian Monsoon. *Global and Planetary Change*, 208, 103729. <https://doi.org/10.1016/j.gloplacha.2021.103729>
- Lee, K., Matsuno, T., Endoh, T., Ishizaka, J., Zhu, Y., Takeda, S., & Sukigara, C. (2017). A role of vertical mixing on nutrient supply into the subsurface chlorophyll maximum in the shelf region of the East China Sea. *Continental Shelf Research*, 143, 139–150. <https://doi.org/10.1016/j.csr.2016.11.001>
- Li, J., Wei, H., Zhang, Z., & Lu, Y. (2013). A modelling study of inter-annual variation of Kuroshio intrusion on the shelf of East China Sea. *Journal of Ocean University of China*, 12(4), 537–548. <https://doi.org/10.1007/s11802-013-2203-z>
- Liang, C., & Xian, W. (2018). Changjiang nutrient distribution and transportation and their impacts on the Estuary. *Continental Shelf Research*, 165, 137–145. <https://doi.org/10.1016/j.csr.2018.05.001>
- Lin, Z., Wang, X., Xiu, P., Chai, F., & Wu, Q. (2019). Boundary phosphate transport of the East China Sea and its influence on biological process. *Journal of Geoscience and Environment Protection*, 07(09), 79–104. <https://doi.org/10.4236/gep.2019.79007>
- Liu, C., Wang, F., Chen, X., & von Storch, J.-S. (2014). Interannual variability of the Kuroshio onshore intrusion along the East China Sea shelf break: Effect of the Kuroshio Volume Transport. *Journal of Geophysical Research: Oceans*, 119(9), 6190–6209. <https://doi.org/10.1002/2013jc009653>
- Liu, Z., Gan, J., Hu, J., Wu, H., Cai, Z., & Deng, Y. (2021a). Progress on circulation dynamics in the East China Sea and southern yellow sea: Origination, pathways, and destinations of Shelf

771 Currents. *Progress in Oceanography*, 193, 102553.

772 <https://doi.org/10.1016/j.pocean.2021.102553>

773 Liu, Z., Gan, J., Wu, H., Hu, J., Cai, Z., & Deng, Y. (2021b). Advances on coastal and estuarine
774 circulations around the Changjiang estuary in the recent decades (2000–2020). *Frontiers in*
775 *Marine Science*, 8, 615929. <https://doi.org/10.3389/fmars.2021.615929>

776 Lou, X., Shi, A., Xiao, Q., & Zhang, H. (2011). Satellite observation of the Zhejiang coastal
777 upwelling in the East China Sea during 2007-2009. *Proceedings of SPIE*, 8175, 283–304.
778 <https://doi.org/10.1117/12.898140>

779 Lü, X. G., Qiao, F. L., Xia, C. S., & Yuan, Y. L. (2007). Tidally induced upwelling off Yangtze
780 River estuary and in Zhejiang coastal waters in summer. *Science in China Series D: Earth*
781 *Sciences*, 50(3), 462–473. <https://doi.org/10.1007/s11430-007-2050-0>

782 Lyu, W., Sun, Q., Wang, S., & Li, B. (2020). Summer vertical turbulent nitrate flux in the
783 Yellow Sea and the East China Sea. *Oceanologia et Limnologia Sinica (in Chinese)*, 51(6),
784 1379–1390.

785 Mellor, G. (2003). The three-dimensional current and surface wave equations. *Journal of*
786 *Physical Oceanography*, 33(9), 1978–1989. [https://doi.org/10.1175/1520-](https://doi.org/10.1175/1520-0485(2003)033<1978:ttcasw>2.0.co;2)
787 [0485\(2003\)033<1978:ttcasw>2.0.co;2](https://doi.org/10.1175/1520-0485(2003)033<1978:ttcasw>2.0.co;2)

788 Menge, B. A., & Menge, D. N. L. (2013), Dynamics of coastal meta-ecosystems: the intermittent
789 upwelling hypothesis and a test in rocky intertidal regions. *Ecological Monographs*, 83, 283–
790 310. <https://doi.org/10.1890/12-1706.1>

791 Miyazawa, Y., Zhang, R., Guo, X., Tamura, H., Ambe, D., Lee, J.-S., et al. (2009). Water mass
792 variability in the western North Pacific detected in a 15-year eddy resolving ocean reanalysis.
793 *Journal of Oceanography*, 65(6), 737–756. <https://doi.org/10.1007/s10872-009-0063-3>

- 794 Ningsih, N. S., Rakhmaputeri, N., & Harto, A. B. (2013). Upwelling variability along the
795 southern coast of Bali and in Nusa tenggara waters. *Ocean Science Journal*, 48(1), 49–57.
796 <https://doi.org/10.1007/s12601-013-0004-3>
- 797 Nykjær, L., & Van Camp, L. (1994). Seasonal and interannual variability of coastal upwelling
798 along Northwest Africa and Portugal from 1981 to 1991. *Journal of Geophysical Research*,
799 99(C7), 14197–14207. <https://doi.org/10.1029/94jc00814>
- 800 Picado, A., Alvarez, I., Vaz, N., Varela, R., Gomez-Gesteira, M., & Dias, J. M. (2014).
801 Assessment of chlorophyll variability along the northwestern coast of Iberian Peninsula. *Journal*
802 *of Sea Research*, 93, 2–11. <https://doi.org/10.1016/j.seares.2014.01.008>
- 803 Ramanantsoa, J. D., Krug, M., Penven, P., Rouault, M., & Gula, J. (2018). Coastal upwelling
804 south of Madagascar: Temporal and spatial variability. *Journal of Marine Systems*, 178, 29–37.
805 <https://doi.org/10.1016/j.jmarsys.2017.10.005>
- 806 Ryu, J.-H., Han, H.-J., Cho, S., Park, Y.-J., & Ahn, Y.-H. (2012). Overview of geostationary
807 ocean color imager (GOCI) and GOCI Data Processing System (GDPS). *Ocean Science Journal*,
808 47(3), 223–233. <https://doi.org/10.1007/s12601-012-0024-4>
- 809 Shan, X., Jin, X., Zhou, Z., & Dai, F. (2011). Fish community diversity in the middle continental
810 shelf of the East China Sea. *Chinese Journal of Oceanology and Limnology*, 29(6), 1199–1208.
811 <https://doi.org/10.1007/s00343-011-0321-2>
- 812 Skogen, M. D., & Søiland H. (1998). *A user's guide to NORWECOM v2.0. The norwegian*
813 *ecological model system*. Bergen, Norway: Institute of Marine Research.
- 814 Strutton, P. G., Chavez, F. P., Dugdale, R. C., & Hogue, V. (2004). Primary productivity in the
815 central equatorial Pacific (3°S 130°W) during GasEx-2001. *Journal of Geophysical Research*,
816 109, C08S06. <https://doi.org/10.1029/2003JC001790>

- Sun, Y., Dong, C., He, Y., Yu, K., Renault, L., & Ji, J. (2016). Seasonal and interannual variability in the wind-driven upwelling along the southern East China Sea Coast. *IEEE Journal of Selected Topics in Applied Earth Observations and Remote Sensing*, 9(11), 5151–5158. <https://doi.org/10.1109/jstars.2016.2544438>
- Sydeman, W. J., García-Reyes, M., Schoeman, D. S., Rykaczewski, R. R., Thompson, S. A., Black, B. A., & Bograd, S. J. (2014). Climate change and wind intensification in coastal upwelling ecosystems. *Science*, 345(6192), 77–80. <https://doi.org/10.1126/science.1251635>
- Tan, S., & Shi, G. (2006). Satellite-derived primary productivity and its spatial and temporal variability in the China Seas. *Journal of Geographical Sciences*, 16(4), 447–457. <https://doi.org/10.1007/s11442-006-0408-4>
- van Ruth, P. D., Patten, N. L., Doubell, M. J., Chapman, P., Rodriguez, A. R., & Middleton, J. F. (2018). Seasonal- and event-scale variations in upwelling, enrichment and primary productivity in the Eastern Great Australian Bight. *Deep Sea Research Part II: Topical Studies in Oceanography*, 157-158, 36–45. <https://doi.org/10.1016/j.dsr2.2018.09.008>
- Villanoy, C., Cabrera, O., Yniguez, A., Camoying, M., de Guzman, A., David, L., & Flament, P. (2011). Monsoon-driven coastal upwelling off Zamboanga Peninsula, Philippines. *Oceanography*, 24(01), 156–165. <https://doi.org/10.5670/oceanog.2011.12>
- Wang, B. (2006). Cultural eutrophication in the Changjiang (Yangtze river) plume: History and perspective. *Estuarine, Coastal and Shelf Science*, 69(3-4), 471–477. <https://doi.org/10.1016/j.ecss.2006.05.010>
- Wang, B., & Wang, X. (2007). Chemical hydrography of coastal upwelling in the East China Sea. *Chinese Journal of Oceanology and Limnology*, 25(1), 16–26. <https://doi.org/10.1007/s00343-007-0016-x>

- 840 Wang, B., Wang, X., & Zhang, R. (2003). Nutrient conditions in the Yellow sea and the east
841 China sea. *Estuarine Coastal Shelf Sciences*, 58(1), 127–136. [https://doi.org/10.1016/S0272-](https://doi.org/10.1016/S0272-7714(03)00067-2)
842 [7714\(03\)00067-2](https://doi.org/10.1016/S0272-7714(03)00067-2)
- 843 Wang, D., Gouhier, T. C., Menge, B. A., & Ganguly, A. R. (2015). Intensification and spatial
844 homogenization of coastal upwelling under climate change. *Nature*, 518(7539), 390–394.
845 <https://doi.org/10.1038/nature14235>
- 846 Wang, D., Wang, H., Li, M., Liu, G., & Wu, X. (2013). Role of Ekman transport versus Ekman
847 pumping in driving summer upwelling in the South China Sea. *Journal of Ocean University of*
848 *China*, 12, 355–365. <https://doi.org/10.1007/s11802-013-1904-7>
- 849 Wang, Q., Guo, X., & Takeoka, H. (2008). Seasonal variations of the Yellow River Plume in the
850 Bohai Sea: A model study. *Journal of Geophysical Research*, 113, C08046.
851 <https://doi.org/10.1029/2007jc004555>
- 852 Wang, Y., Guo, X., Zhao, L., & Zhang, J. (2019). Seasonal variations in nutrients and biogenic
853 particles in the upper and lower layers of East China Sea Shelf and their export to adjacent seas.
854 *Progress in Oceanography*, 176, 102138. <https://doi.org/10.1016/j.pocean.2019.102138>
- 855 Wei, Q., Yao, P., Xu, B., Zhao, B., Ran, X., Zhao, Y., et al. (2021). Coastal upwelling combined
856 with the river plume regulates hypoxia in the Changjiang estuary and adjacent Inner East China
857 Sea shelf. *Journal of Geophysical Research: Oceans*, 126(11), e2021JC017740.
858 <https://doi.org/10.1029/2021jc017740>
- 859 Xie, L., & Hsieh, W. W. (1995). The global distribution of wind-induced upwelling. *Fisheries*
860 *Oceanography*, 4, 52–67. <https://doi.org/10.1111/j.1365-2419.1995.tb00060.x>

- 861 Xu, L., Yang, D., Benthuisen, J. A., & Yin, B. (2018). Key dynamical factors driving the
862 Kuroshio subsurface water to reach the Zhejiang Coastal Area. *Journal of Geophysical*
863 *Research: Oceans*, 123(12), 9061–9081. <https://doi.org/10.1029/2018jc014219>
- 864 Xu, L., Yang, D., Greenwood, J., Feng, X., Gao, G., Qi, J., et al. (2020). Riverine and oceanic
865 nutrients govern different algal bloom domain near the Changjiang estuary in Summer. *Journal*
866 *of Geophysical Research: Biogeosciences*, 125(10), e2020JG005727.
867 <https://doi.org/10.1029/2020jg005727>
- 868 Xu, Q., Wang, S., Sukigara, C., Goes, J. I., Gomes, H. do, Matsuno, T., et al. (2022). High-
869 resolution vertical observations of phytoplankton groups derived from an in-situ fluorometer in
870 the East China Sea and Tsushima Strait. *Frontiers in Marine Science*, 8, 756180.
871 <https://doi.org/10.3389/fmars.2021.756180>
- 872 Xu, Q., Zhang, S., Cheng, Y., & Zuo, J. (2017). Interannual feature of summer upwelling around
873 the Zhoushan Islands in the East China Sea. *Journal of Coastal Research*, 331, 125–134.
874 <https://doi.org/10.2112/jcoastres-d-15-00197.1>
- 875 Yang, D., Yin, B., Liu, Z., & Feng, X. (2011). Numerical study of the ocean circulation on the
876 East China Sea shelf and a Kuroshio bottom branch northeast of Taiwan in summer. *Journal of*
877 *Geophysical Research*, 116, C05015. <https://doi.org/10.1029/2010JC006777>
- 878 Yang, D., Yin, B., Sun, J., & Zhang, Y. (2013). Numerical Study on the origins and the forcing
879 mechanism of the phosphate in upwelling areas off the coast of Zhejiang Province, China in
880 Summer. *Journal of Marine Systems*, 123-124, 1–18.
881 <https://doi.org/10.1016/j.jmarsys.2013.04.002>
- 882 Yang, S., Mao, X., & Jiang, W. (2020). Interannual Variation of Coastal Upwelling in Summer
883 in Zhejiang, China. *Periodical of Ocean University of China (in Chinese)*, 50(2), 1–8.

- Yin, W., & Huang, D. (2019). Short-term variations in the surface upwelling off northeastern Taiwan observed via satellite data. *Journal of Geophysical Research: Oceans*, 124(2), 939–954. <https://doi.org/10.1029/2018jc014537>
- Yu, Z. (2014). *Characteristics of nutrient in the southern Yellow Sea and northern East China Sea from 2011 to 2013*, (Master's thesis in Chinese). Retrieved from CNKI. (<https://kns.cnki.net/KCMS/detail/detail.aspx?dbname=CMFD201501&filename=1014204213.nh>). Qingdao, China: Ocean University of China.
- Yue, J., Noman, M. A., & Sun, J. (2021). Kuroshio intrusion drives the *trichodesmium* assemblage and shapes the phytoplankton community during spring in the East China Sea. *Journal of Oceanology and Limnology*, 39(2), 536–549. <https://doi.org/10.1007/s00343-020-9344-x>
- Zhang, J., Guo, X., & Zhao, L. (2019). Tracing external sources of nutrients in the East China Sea and evaluating their contributions to primary production. *Progress in Oceanography*, 176, 102122. <https://doi.org/10.1016/j.pocean.2019.102122>
- Zhao, B., Yao, P., Bianchi, T. S., Arellano, A. R., Wang, X., Yang, J., et al. (2018). The remineralization of sedimentary organic carbon in different sedimentary regimes of the yellow and East China Seas. *Chemical Geology*, 495, 104–117. <https://doi.org/10.1016/j.chemgeo.2018.08.012>
- Zhao, L., & Guo, X. (2011). Influence of cross-shelf water transport on nutrients and phytoplankton in the East China Sea: A model study. *Ocean Science*, 7(1), 27–43. <https://doi.org/10.5194/os-7-27-2011>

- 905 Zhou, F., Xue, H., Huang, D., Xuan, J., Ni, X., Xiu, P., & Hao, Q. (2015). Cross-shelf exchange
906 in the shelf of the East China Sea. *Journal of Geophysical Research: Oceans*, 120(3), 1545–
907 1572. <https://doi.org/10.1002/2014jc010567>
- 908 Zhou, P., Song, X., Yuan, Y., Wang, W., Chi, L., Cao, X., & Yu, Z. (2018). Intrusion of the
909 Kuroshio Subsurface Water in the Southern East China Sea and its variation in 2014 and 2015
910 traced by dissolved inorganic iodine species. *Progress in Oceanography*, 165, 287–298.
911 <https://doi.org/10.1016/j.pocean.2018.06.011>